Airfoil Trailing-edge Noise Reduction using Flow Suction

Luana Maciel Cesar*, Hasan Kamliya Jawahar†, Mahdi Azarpeyvand‡
University of Bristol, Bristol, United Kingdom, BS8 1TR

Large eddy simulations were carried out for a NACA-0012 airfoil with trailing edge flow suction at the angle of attack $\alpha = 0°$ for a chord-based Reynolds number of $Re_c = 4 \times 10^5$. Simulations were performed with different flow suction rates to demonstrate the viability of the technique. The baseline case was thoroughly validated with experimental data. The aerodynamic and aeroacoustic characteristics of the boundary layer and wake were studied in detail for different flow suction rates. The mean velocity results showed reduced wake velocity deficit. Results have also shown that the suction of the boundary flow upstream of the trailing edge can reduce the boundary layer and wake turbulent kinetic energy and significant reduction of the wall pressure spectra near the trailing edge. The effect of flow suction on the spanwise correlation length has also been studied. The results have shown that a moderate flow suction rate can result in partial flow laminarization, broadband reduction of the surface pressure spectra and the radiated noise from the trailing edge.

Nomenclature

FS	=	Flow Suction
LES	=	Large Eddy Simulation
$RANS$	=	Reynolds Averaged Navier Stokes Simulation
c	=	chord length, m
f	=	frequency, Hz
l	=	span length, m
p_{ref}	=	reference pressure (= 2×10^5), Pa
Re_c	=	chord based Reynolds number
RMS	=	root mean squared
k	=	turbulence kinetic energy, m^2/s^2
U_∞	=	free stream velocity, m/s
$\overline{u'u'}$	=	streamwise Reynolds normal stress component
$\overline{v'v'}$	=	crosswise Reynolds normal stress component
x, y, z	=	streamwise, crosswise, spanwise Cartesian coordinates, m
α	=	angle of attack, °
$\gamma^2_{p_i p_j}$	=	coherence function
Φ_{pp}	=	wall-pressure power spectral density, Pa^2/Hz
C_μ	=	flow suction momentum coefficient
U_{jet}	=	flow suction velocity , m/s
b	=	flow suction slot, m
Θ_0	=	boundary layer momentum thickness, m
PSD	=	Power Spectral Density, m
$Pdyn$	=	dynamic pressure, Pa
τ	=	shear stress, N/m^2
ω	=	frequency, rad/s

*PhD Student, Department of Mechanical Engineering, AIAA Student Member, lm15898@bristol.ac.uk
†PhD Student, Department of Aerospace Engineering, AIAA Student Member, hasan.kj@bristol.ac.uk
‡Reader in Aeroacoustics, Department of Mechanical Engineering, m.azarpeyvand@bristol.ac.uk

I. Introduction

AIRFOIL trailing edge noise has been a long-standing problem when it comes to airfoil self-noise. Among all the airfoil self-noise mechanism listed: vortex shedding noise, separation stall noise, tip vortex formation noise and trailing edge noise on turbulent boundary layer [1], the trailing edge noise has been a major concern since the turbulent boundary layers are more likely to develop on the vast majority of aircrafts and wind turbine applications.

Several studies on airfoil trailing edge treatments have been carried out in the past in order to attenuate the noise generated by them. The predominantly used methods can be classified into passive and active flow control methods. For Passive flow control approach, no external energy is added to alter the boundary layer. The changes to the flow characteristics are introduced by adding devices like serrations [2–5], types of riblets, morphing [6–10] or by applying porous [11–13] and compliant materials. whereas, for the active flow control method [14] external energy is added to the flow. The main advantage of this method includes the ability to control the flow actively to obtain a broad range of effects by using a small and localized momentum input. Other advantages include the possibility to improve the airfoil performance including lift increment, drag reduction, heat transfer, mixing and noise minimization [15]. A wide range of applications would benefit when it comes to delaying or advancing to boundary layer transition, triggering or ceasing turbulence and delaying or initiating separation [15]. The active flow control studies primarily focus on the aerodynamics and aeroacoustic improvements by steady flow suction and blowing on airfoils [17–19] and the circulation control, the coanda effect [16–19].

The energy requirement for active flow control methods have remained as an expensive problem. While the energy expenditure on flow control techniques for aerodynamics applications scales with the use of 10-6 of the system's energy, the energy scale required on aeroacoustics applications is just 10-3. Therefore, the use of active flow control for noise suppression is of great interest among the researchers. The most of the available research on airfoil noise reduction by flow manipulation has been carried out using passive techniques while just a few works has investigated the noise suppression by active flow control technology.

Computational studies are often favoured when it comes to active flow application due to the complexities and expenses involved with the experiments. Large Eddy Simulations (LES) study on the application of trailing edge blowing by Winkle et al. [20] showed that airfoil self-noise rises for frequencies higher than 2kHz as a result of the jet interaction with the trailing edge while for frequencies lower than 2kHz the wake-airfoil interaction noise has been reduced due the wake turbulence lowering.

In this paper we have investigate the trailing edge flow suction (FS) on a NACA 0012 airfoil trailing edge and its influence on the broadband noise sources. A high fidelity LES computational study was carried out in order to understand the aerodynamic and aeracoustic effects of the flow suction at the trailing edge. The LES results of the baseline case has been thoroughly validated with existing experimental results. The LES for FS case was then carried out with the same computational setup with the flow-suction activated on the baseline case. The FS was placed over the region $0.878 < x/c < 0.925$ for 4 different momentum coefficients and the results have been compared with the baseline case with no suction as reference. The results were then used to investigate the steady and unsteady pressure, boundary layer development, wake development and broadband noise sources occurring on a single airfoil with FS. The structure of the following paper is as follows. The airfoil geometry with the tripping device and the computational domain are presented and explained in Sec. II. The aerodynamic results of pressure coefficient, boundary layer and wake measurements are presented and discussed in Sec. III. The aerocoustic results including wall-pressure spectra, spanwise correlation of pressure and far-field noise are presented and discussed in Sec. IV.

II. Large-Eddy Simulation

Large-Eddy Simulations were performed for a NACA0012 airfoil with and without trailing edge flow suction (FS) at angle of attack $\alpha = 0°$. In all the configurations, turbulent flow was triggered by steady suction and blowing tripping device. The simulations were performed in OpenFoam 2.2 using dynamic Smagorinsky sub-grid scale model. The Baseline results were validated with experimental data from Sagrado and Hynes [21] for a chord-based Reynolds number $Re_c = 4 \times 10^5$. The details of the computational setup, numerical method and flow solvers, grid topologies and boundary conditions are presented in the following subsections.

A. Computational Model Setup

The NACA 0012 airfoil has a chord length of $c = 0.2$ m and span length $l = 0.02$ m. The simulations were carried out for an angle of attack $\alpha = 0°$ at freestream velocity of $U_\infty = 30$ m/s, corresponding to a chord based Reynolds number of $Re_c = 4 \times 10^5$. For both the baseline and the FS cases, turbulent flow was triggered by applying steady flow suction and blowing into the boundary layer. Tripping devices were placed on both the suction and the pressure side [22] of the airfoil, in order to achieve turbulent flow, steady suction was applied over the streamwise

region $0.150 < x/c < 0.175$ and steady blowing over the streamwise region $0.175 < x/c < 0.200$. The results from a simulation of flow past a cylinder [23] have shown that partial tripping performed better boundary layer transition when compared with full span tripping. Wolf *et. al* [22] has shown that boundary layer transition can be accomplished by applying a constant steady suction and blowing over the spanwise region $0.01 < z/c < 0.09$ with a flow velocity of $|U_{blowing}| = |U_{suction}| = 0.03U_\infty$. The same pattern was found by testing both configurations (full and partial span tripping) on the present simulations and therefore the partial span tripping device was used for all the presented simulations. The Flow Suction (FS) airfoil has a suction slot that was placed close to trailing-edge over the region $0.878 < x/c < 0.925$ where for the different FS cases, different flow suction magnitudes are applied as defined in Table 1. The schematic of the tripping device and the suction slot on the FS airfoil is shown in Fig. 1a. The top view of the airfoil schematic is shown in Fig. 1b.

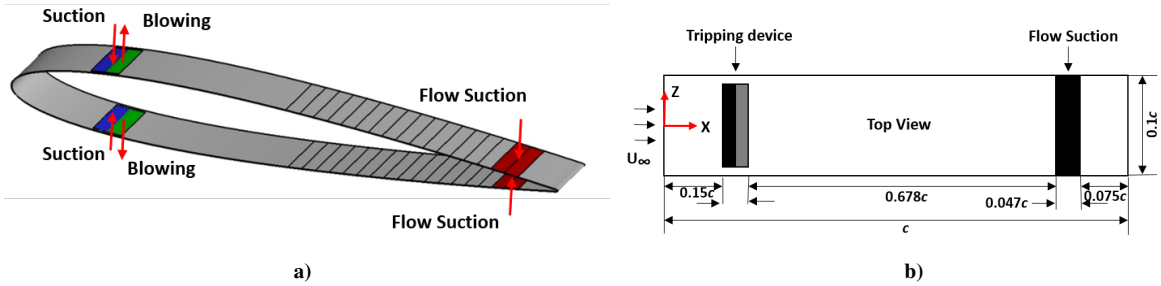

Figure 1. (a) Schematic of the boundary conditions applied on the NACA 0012 airfoil (b) Top view of the NACA 0012 airfoil.

Table 1. Flow suction rates near the trailing edge.

Cases	C_μ	$U_{jet}[m/s]$	U_{jet}/U_∞
Baseline	0	0	0
Case 1	0.1	0.9147	3.05
Case 2	0.3	2.774	9.25
Case 3	1.2	10.97	36.57

B. Grid Topology and Boundary Conditions

A block-structured C-mesh for both the baseline and the Flow Suction (FS) cases were generated using a commercial software ANSYS ICEM-CFD. In order to capture the boundary layer accurately, finer grids were concentrated closer to the airfoil surface containing 6 nodes within $\Delta y^+ \approx 5$ and a suitable stretching factor of 1.2 was applied to ensure numerical stability. The computational domain had a dimension of $L_x \times L_y \times L_z = 10c \times 10c \times 0.1c$. In the airfoil streamwise direction, 1416 cells were placed. In order to capture the flow accurately over the airfoil surface the mesh refinement was made twice that of the far-field in the streamwise and spanwise direction as shown in Fig. 2b. This resulted with a cell distribution of $L_x \times L_y \times L_z = 2256 \times 520 \times 64$ corresponding to the streamwise, crosswise and spanwise direction, respectively. This resulted in a mesh resolution of $\Delta x^+ \approx 40$, $\Delta y^+ \approx 0.5 - 1.0$ and $\Delta z^+ \approx 20$. The far-field region had a cell distribution of $L_x \times L_y \times L_z = 1218 \times 260 \times 32$ ($\Delta x^+ \approx 80$ and $\Delta z^+ \approx 40$). The no-slip boundary conditions were used over the airfoil surfaces except the tripping device and at the flow suction slot close to the trailing edge for the FS cases. Periodic boundary conditions were applied in the spanwise direction and zero-gradient was used for the top, bottom, and outlet of the computational domain. The different momentum coefficients (C_μ) used in the present study are defined in Equation 1 and shown in Table 1.

$$C_\mu = \frac{U_{jet}.b}{U_\infty.\Theta_0} \tag{1}$$

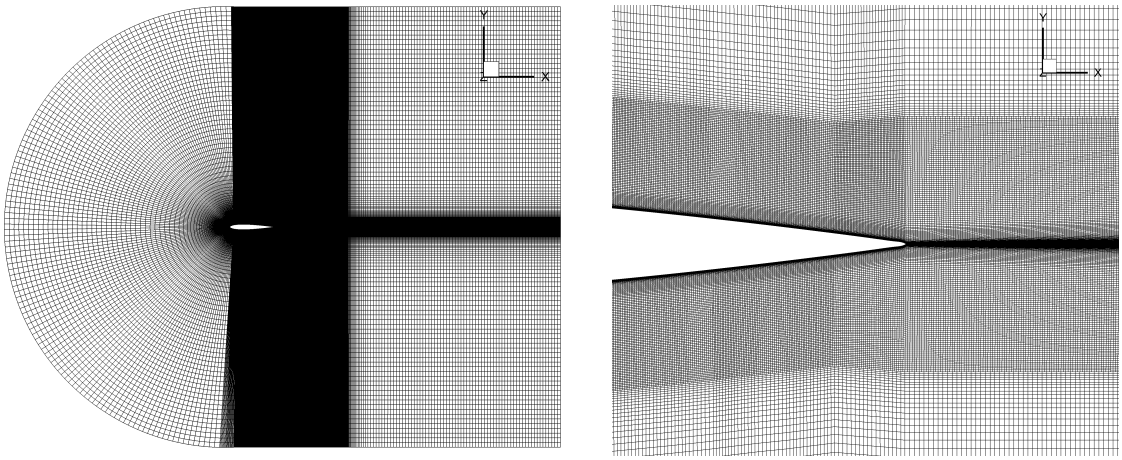

a) b)

Figure 2. C-type mesh over the complete domain (a) and mesh quality near the trailing-edge (b).

C. Numerical Method

Incompressible Large Eddy Simulations (LES) of a subsonic flow past the NACA0012 airfoil were performed. The simulations were carried out on OpenFoam 2.2 opensource CFD software based on Finite Volume discretization of Gaussian integration. Reynolds Averaged Navier Stokes simulations (RANS) using SpalartAllmaras turbulence model were used to initiate the LES. For the RANS simulations, a second-order accuracy scheme was used for the pressure and velocity gradient discretization and the Gaussian central differencing for linear interpolation was used. The divergence of the convective terms was discretized using a bounded gaussian upwind scheme and the diffusive terms using a Gaussian linear scheme. An explicit non-orthogonal correction scheme was used to calculate the surface normal gradient. The SIMPLE solver was used for the RANS. For the LES simulations, a second-order accuracy scheme for velocity and pressure gradients were used. The divergence of the convective and diffusive terms and laplacian schemes were of second-order accuracy. For the time discretization, a second-order backward-differencing scheme was employed. The PIMPLE solver (merged PISO-SIMPLE) algorithm was used for the LES. The dynamic subgrid-scale eddy viscosity model proposed by Lilly (1992) [24] was applied as a closure model. The simulations were carried out for 25 airfoil flow-through times and the data was collected for the last 10 airfoil flow-through times.

III. Results and Discussion

A. NACA 0012 Baseline Validation at angle of attack $\alpha = 0^\circ$

The LES of the baseline NACA 0012 airfoil was validated with available experimental data [21] for a chord based Reynolds number of $Re_c = 4 \times 10^5$. The results of the pressure coefficient (C_p) are presented in Fig. 3a and the results of the boundary layer displacement and momentum thickness are shown in Fig. 3b. The LES results show a good agreement with the experiments. A trip wire was used in the experiments [21] to trigger the boundary layer turbulence. The boundary layer trip was incorporated into the simulations using a suction and blowing flows. The results of the C_p show an increased pressure at the tripping device location with a good agreement downstream of the tripping device.

The results of the boundary layer displacement and momentum thickness show negligible difference compared to the experimental results at location $x/c = 0.75 - 0.90$. At further downstream locations, $x/c > 0.90$, the region of interest, the differences become insignificant. The negligible differences at the upstream locations were due to the different streamwise locations of the tripping device between the experiments and the simulations. The boundary layer thickness parameter used in the calculations to obtain the boundary layer displacement and boundary layer momentum thickness parameters were calculated corresponding to Sagrado and Hynes [21]. The edges of the boundary layer were considered at the point where the velocity profiles of the simulation was 99.5% of the profiles obtained by linear interpolation.

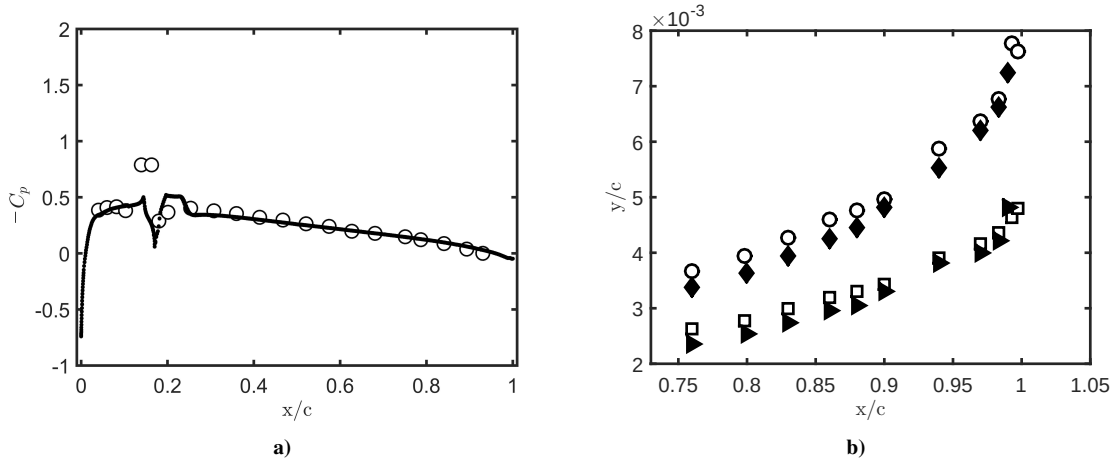

Figure 3. (a) Pressure coefficient (LES —, Exp ○) (b) boundary layer momentum thickness (LES ▷, Exp □) and displacement thickness (LES ◇, Exp ○) [21].

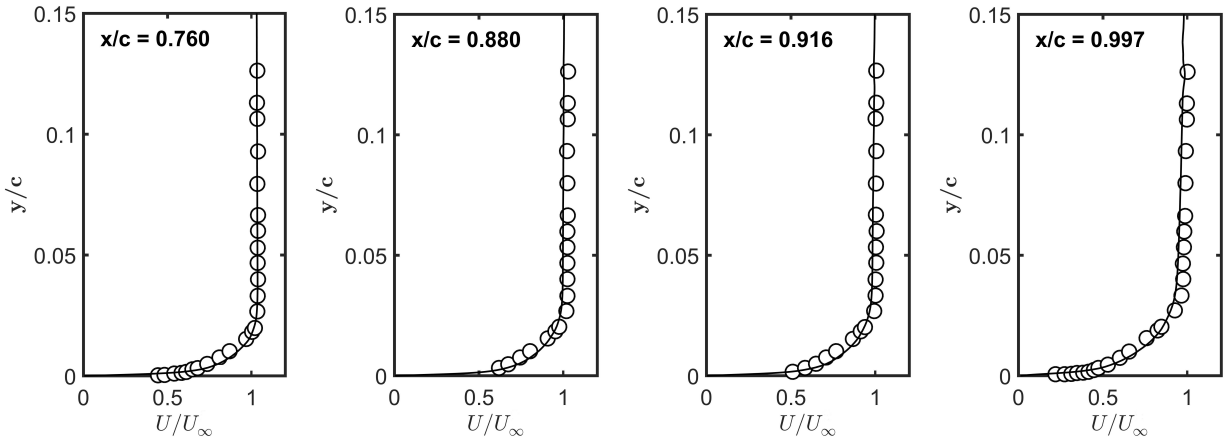

Figure 4. Mean velocity profiles at various streamwise locations on the boundary layer of the NACA 0012 baseline airfoil for LES — and Exp ○ [21].

The non-dimensionalised mean velocity profiles at various streamwise locations along the airfoil surface and at near wake location $x/c = 1.01$ are presented in Fig. 4 and 5, respectively along with the experimental data [21]. The results of the mean velocity profiles from the simulations validate well with the experiments. The Reynolds stresses $\overline{u'u'}$ and $\overline{v'v'}$ for various streamwise locations are shown in Fig. 6 and 6b, respectively. The maximum values for $\overline{u'u'}$ and $\overline{v'v'}$ are observed close to the airfoil surface with increasing magnitude at the measurement locations closer to the airfoil trailing edge. The results of the Reynolds stresses at the boundary layer validates reasonably well with the experimental measurements except in the near wall region where experiments are difficult. The wall pressure power spectral density for the locations $x/c = 0.80$, $x/c = 0.90$ and $x/c = 0.98$ at the airfoil surface are presented in Fig. 7a for the current LES and the experiments [21] in Fig. 7b. The results from the simulations agrees well with the experimental study.

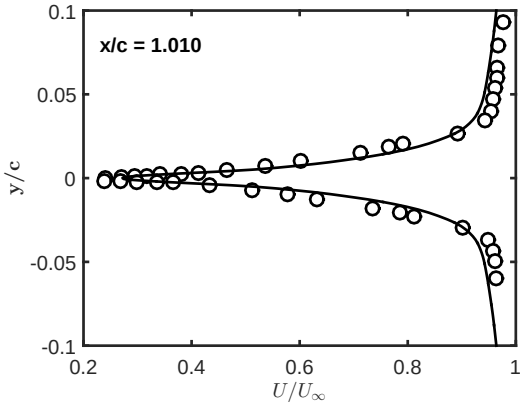

Figure 5. Wake profile at the vicinity of the trailing-edge of the NACA 0012 baseline airfoil for LES — and Exp ∘ [21].

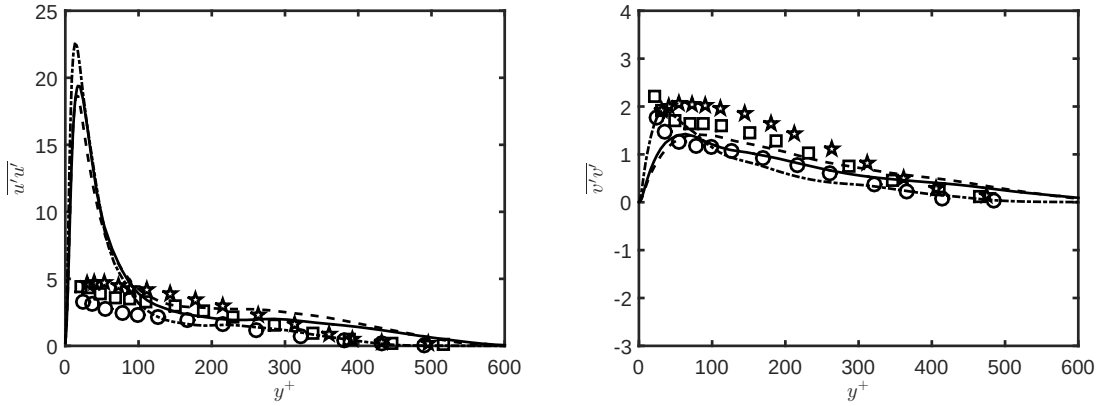

a) Reynolds Stresses $\overline{u'u'}$ **b) Reynolds Stresses $\overline{v'v'}$**

Figure 6. (a) Streamwise normal Reynolds stresses $\overline{u'u'}$ and (b) crosswise normal Reynolds stresses $\overline{v'v'}$ for LES x/c = 0.80 - - -, x/c = 0.90 —, x/c = 0.98 - . - and Exp x/c = 0.80 ∘, x/c = 0.90 □, x/c = 0.98 ⋆.

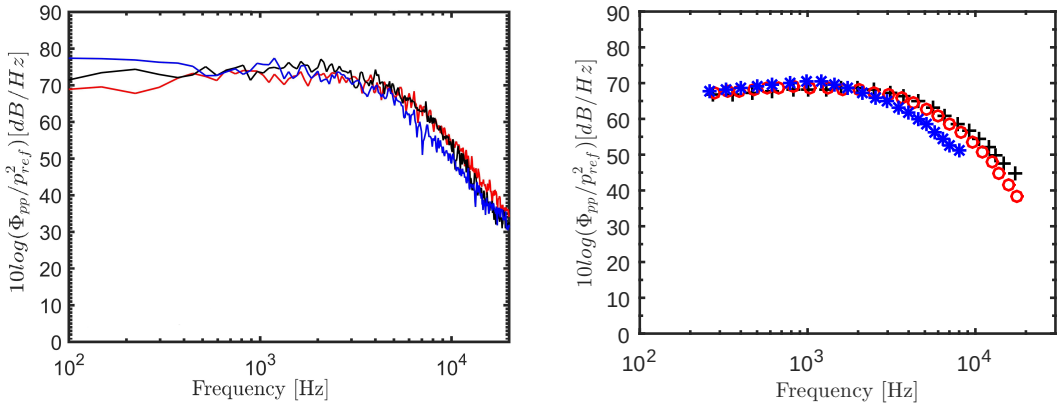

a) LES **b) Exp [21]**

Figure 7. Wall-pressure power spectral density with $P_{ref} = 2 \times 10^5$ Pa at various streamwise locations. a) LES (x/c =0.80) —,(x/c=0.90) —, and (x/c=0.98) —, b) Experiments (x/c =0.80) black cross, (x/c=0.90) red circle, and (x/c=0.98) blue asterisk.

B. Flow Suction for NACA 0012 at angle of attack $\alpha = 0°$

The fundamental purpose of this study is to investigate the effects of suction on the trailing edge noise of a NACA 0012 airfoil. The results for the FS cases with various C_μ (see Table. 1) in comparison with the baseline for an angle of attack of $\alpha = 0°$ are presented in this section.

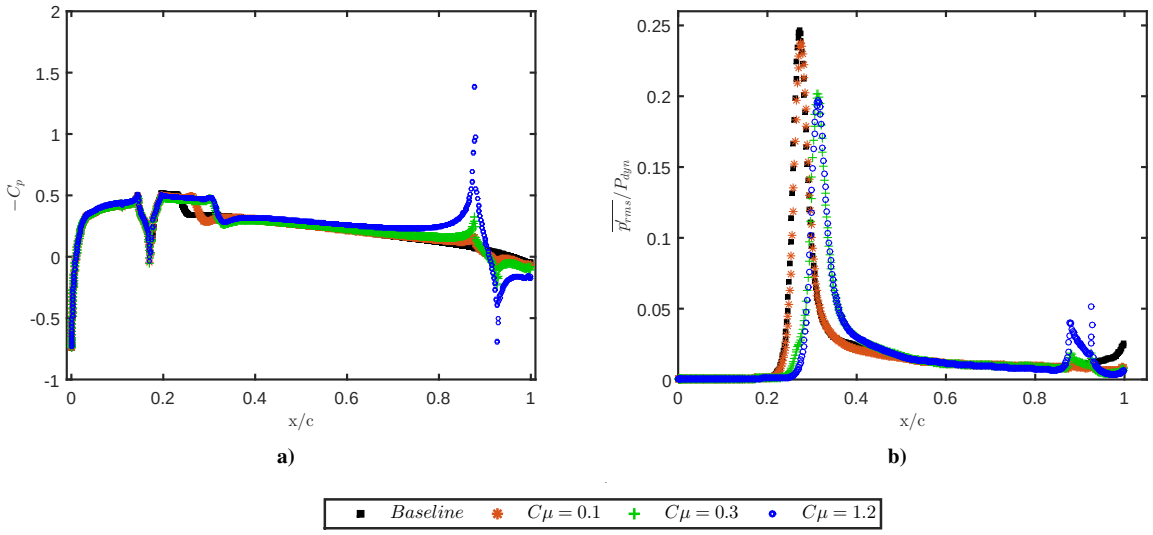

Figure 8. (a) Pressure coefficient (b) unsteady pressure development along the NACA 0012 airfoil chord for baseline .

The non-dimensionalised mean pressure coefficient and the averaged unsteady pressure coefficient along the airfoil chord for the baseline and FS cases are shown in Fig. 8. The mean pressure coefficient in Fig. 8a shows the effects of the flow suction causing discontinuity on the curve at the FS slot location and subsequent mild reduction on the pressure coefficient close to the trailing-edge. The RMS pressure normalized by the dynamic pressure for the FS and baseline configurations presented in Fig 8b shows a substantial reduction in the pressure fluctuations downstream of the flow suction device.

1. *Boundary Layer and Wake Flow Measurements*

The non-dimensionalised mean velocity profile and turbulent kinetic energy (TKE) profiles at the boundary layer of both the Baseline and FS cases are presented in Fig. 10. The results are presented for various streamwise locations $x/c = 0.65, 0.85, 0.89, 0.95, 0.97$ and 0.99. The results are presented for angle of attack $\alpha = 0°$ at freestream velocity $U_\infty = 30$ m/s corresponding to a chord based Reynolds number of $Re_c = 4 \times 10^5$ at mid-span of the computational domain and for various trailing edge flow suction rates Case 1-3, see Table. 1.

The mean velocity results in Fig. 9a show insignificant changes to the boundary layer velocity peak and the velocity gradient $(\delta U/\delta y)$ at location $x/c = 0.65$. The most dominant changes in the boundary layer velocity peak and the velocity gradient was observed at location $x/c = 0.85$, just upstream of the FS slot. At region close to the wall $y/c = 0.1$ at location $x/c = 0.85$, the increase in boundary layer velocity peak and velocity gradient are insignificant for Case 1 relative to the Baseline. For Case 2 and 3, the increase in the boundary layer velocity peak was 6.2% and 15.2% respectively relative to the Baseline for region $y/c = 0 - 0.1$. For crosswise regions $y/c = 0.1 - 0.2$ for Case 2 and 3 the increase in the boundary layer velocity peak was 3.8% and 9% respectively relative to the Baseline. For all the locations downstream of the FS, at $x/c = 0.95, 0.97$ and 0.99, the change in velocity peak is insignificant compared to the Baseline but the velocity gradient increases with increasing intensity in flow suction.

The TKE profiles at the boundary layer are shown in Fig. 9b. The results show insignificant changes in the boundary layer at streamwise location $x/c = 0.65$ as seen earlier in mean velocity profiles. At streamwise location $x/c = 0.85$ the TKE for Cases 1 to 3 reduces by $4.5\%, 20\%$ and 31% relative to the Baseline respectively and at location $x/c = 0.89$, just before the flow suction, the TKE for Cases 1 to 3 reduces by $55\%, 61\%$ and 70% relative to the Baseline respectively. At streamwise locations, $x/c = 0.95, 0.97$ and 0.99, aft of the flow suction, relative to the Baseline the Case 2 has a TKE reduction of $82\%, 84\%$ and 85% and the Case 3 has a TKE reduction of $84\%, 88\%$ and

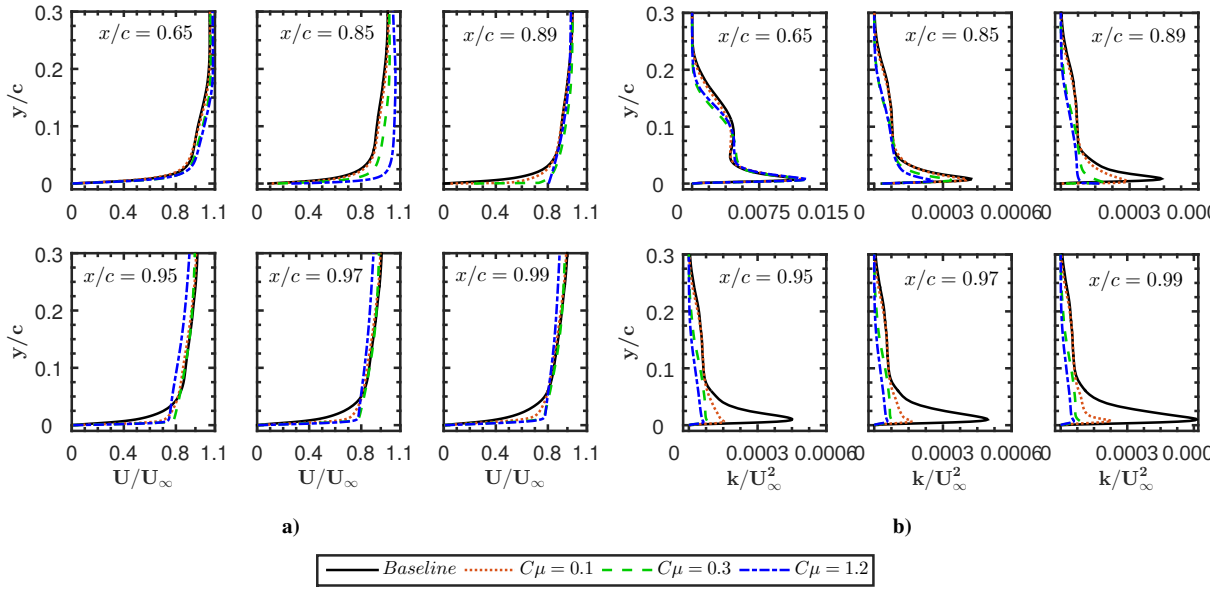

Figure 9. Mean velocity profiles and turbulent kinetic energy at the various streamwise boundary layer locations over the Baseline and FS cases.

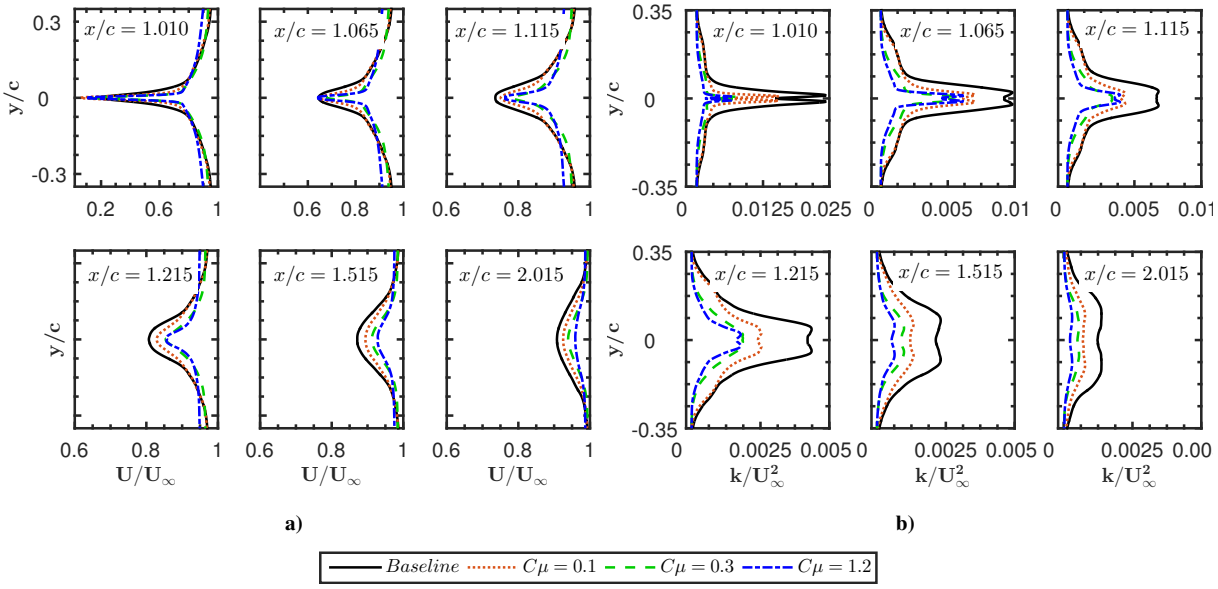

Figure 10. Mean velocity profiles and turbulent kinetic energy at the various wake locations for the Baseline and FS cases.

90% respectively. The results show that the reduction in TKE increases as the flow moves downstream for the Case 2 and 3. For the Case 1, relative to the Baseline, the TKE reduction increases from 66% to 67% at locations $x/c = 0.95$ and 0.97 but the TKE reduction reduces back to 63% at downstream location $x/c = 0.99$. This increased TKE close to the trailing edge for Case 1 suggests it would have slightly increased noise levels relative to Case 2 and 3.

The mean velocity wake profile for the near wake locations $x/c = 1.010, 1.065$ and 1.115 and far wake locations $x/c = 1.215, 1.515$ and 2.015 are presented in Fig. 10a. Results show that the velocity deficit for the FS configuration decreases for all the locations and higher velocity gradient were observed relative to the Baseline. At the near wake locations $x/c = 1.010$ and 1.065, the results show that difference in the peak location of the velocity deficit is insignificant for the Case 1 to 3 compared to the Baseline. The Case 1 to 3 have reduced velocity deficit relative to the Baseline for these near wake locations. The velocity gradient for the Case 1 is closer to the Baseline at the location $x/c = 1.115$. For all the Case 1 to 3, at the location $x/c = 1.215$, 1.515 and $x/c = 2.015$, increased percentage in the reduction of the

velocity deficit peak relative to the Baseline were observed till location $x/c = 1.515$ and it reduced at far wake location $x/c = 2.015$. The highest reduction in velocity deficit peak relative to the Baseline were found at location $x/c = 1.515$ with Case 1 a reduction of 2.6%, Case 2 a reduction of 4.7% and with Case 3 having a highest reduction of 6.6%. The TKE results for the wake profiles are presented in Fig. 10b. A characteristic double-peak behaviour were seen in the wake TKE profiles. The results for FS Case 1 to 3 show reduction in the TKE profile for all the presented wake locations relative to the Baseline. The highest reduction was found at near wake location $x/c = 1.010$ with Case 1, 2 and 3 having TKE reduction of 69%, 75% and 88% relative to the Baseline. The reduction in TKE profiles relative to the Baseline for the Cases 1 to 3 increase at consecutive downstream locations, $x/c = 1.215$, 1.515 and 2.015 for Case 1 it reduces from 42.5% to 43.5%, Case 2 from 56.5% to 59.5% and with highest reductions for Case 3 from 61.2% to 81%.

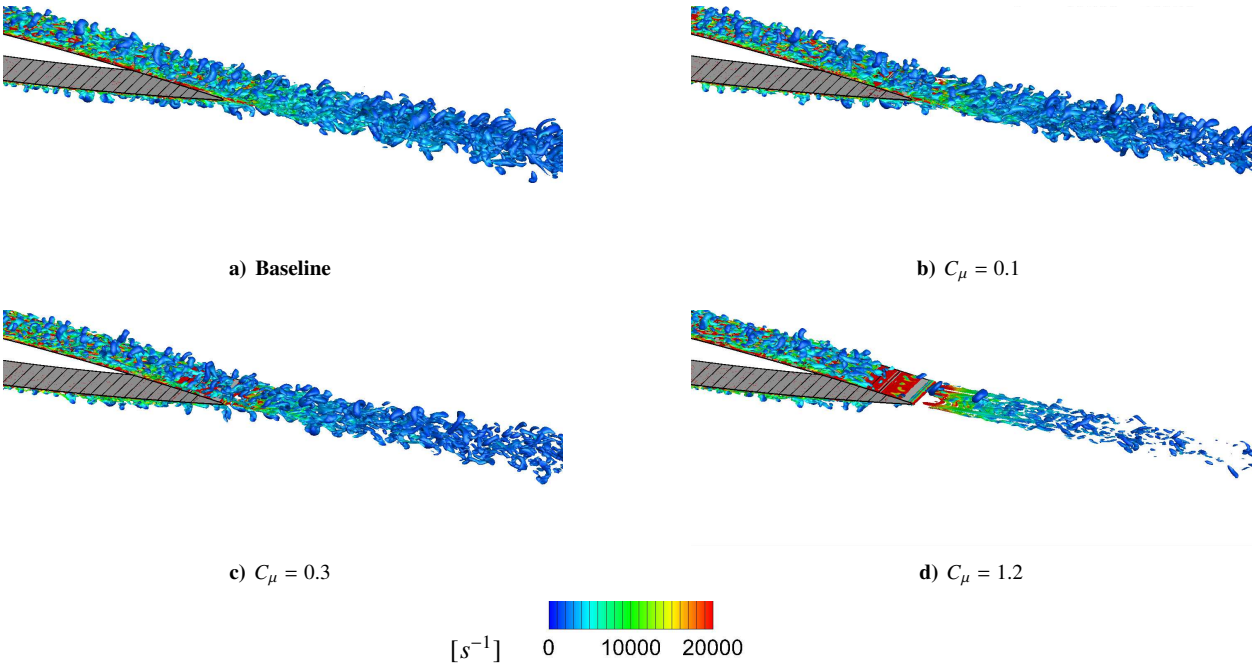

Figure 11. Q criterion coloured by vorticity magnitude for the Baseline and FS cases

2. *Wake Flow Structure*

The second invariant of the velocity-gradient tensor Q-colored by mean vorticity magnitude is presented in Fig. 11. The turbulent boundary layer due to boundary layer trip were seen evidently. Downstream of the FS slot the turbulent structures reduce as the intensity of the flow suction increases compared to the Baseline. For the FS Case 3, the case with highest momentum coefficient $C_\mu = 1.2$, a substantial diminution of the large eddies in the vicinity of the trailing edge can be observed. The FS configuration presents a lesser vorticity magnitude downstream of the flow suction slot containing more coherent structures than on the baseline configuration.

3. *Reynolds Stresses*

The streamwise ($\overline{u'u'}$) and crosswise ($\overline{v'v'}$) Reynolds stress tensor contours for the Baseline and all the FS cases are presented in Fig. 12. The Baseline $\overline{u'u'}$ results show an increased magnitude close to the airfoil wall and the airfoil wake with double peak behavior up until downstream location $x/c = 1.15$. As the intensity of the flow suction is increased for Cases 1 to 3, relative to the Baseline, the thickness and the $\overline{u'u'}$ magnitude of the boundary layer decreases with increasing flow suction and the width of the double peak behavior was also seen to reduce with increasing C_μ.

The highest reduction in $\overline{u'u'}$ magnitude was observed for Case 3, aft of the trailing edge flow suction relative to the Baseline. The $\overline{v'v'}$ results for the Baseline show increased magnitude in the entire boundary layer region up until location $x/c > 0.8$ and at location $x/c < 0.95$ close to the vicinity of the trailing edge through the wake. For the FS Cases 1 to 3 as expected increased reduction in the $\overline{v'v'}$ magnitude with increasing C_μ relative to the Baseline was observed. The reduction in $\overline{v'v'}$ was also seen before location $x/c > 0.8$ but with minimal reduction in magnitude

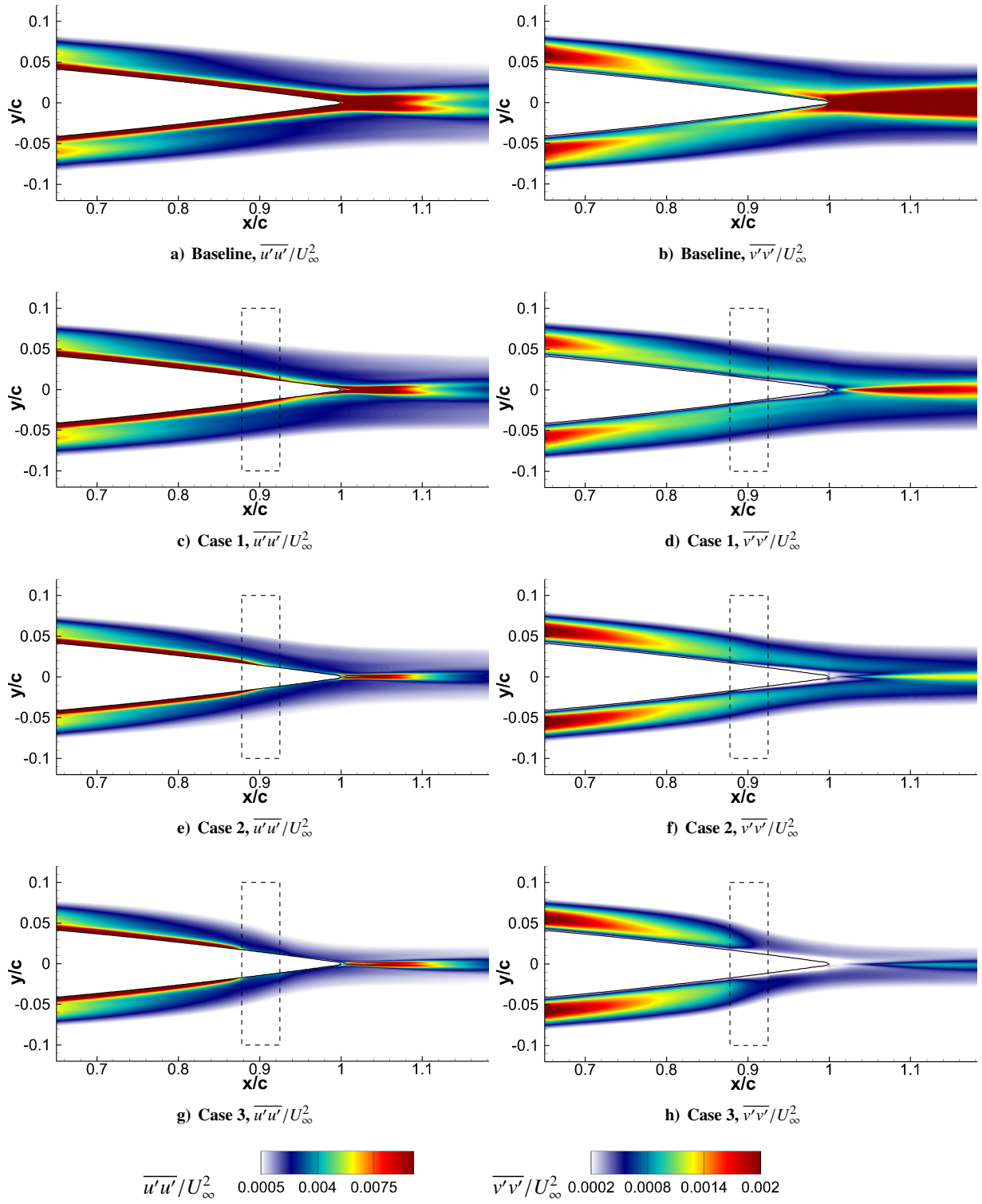

a) **Baseline,** $\overline{u'u'}/U_\infty^2$ b) **Baseline,** $\overline{v'v'}/U_\infty^2$

c) **Case 1,** $\overline{u'u'}/U_\infty^2$ d) **Case 1,** $\overline{v'v'}/U_\infty^2$

e) **Case 2,** $\overline{u'u'}/U_\infty^2$ f) **Case 2,** $\overline{v'v'}/U_\infty^2$

g) **Case 3,** $\overline{u'u'}/U_\infty^2$ h) **Case 3,** $\overline{v'v'}/U_\infty^2$

Figure 12. Streamwise and crosswise Reynolds stress distribution for the Baseline and FS cases.

relative to the Baseline. For the FS Case 3, a substantial reduction in $\overline{v'v'}$ was observed at location $x/c < 0.95$ close to the vicinity of the trailing edge and the wake. The reduced fluctuations close to the airfoil trailing edge with increasing C_μ is an indication of a possible reduction of airfoil trailing edge noise.

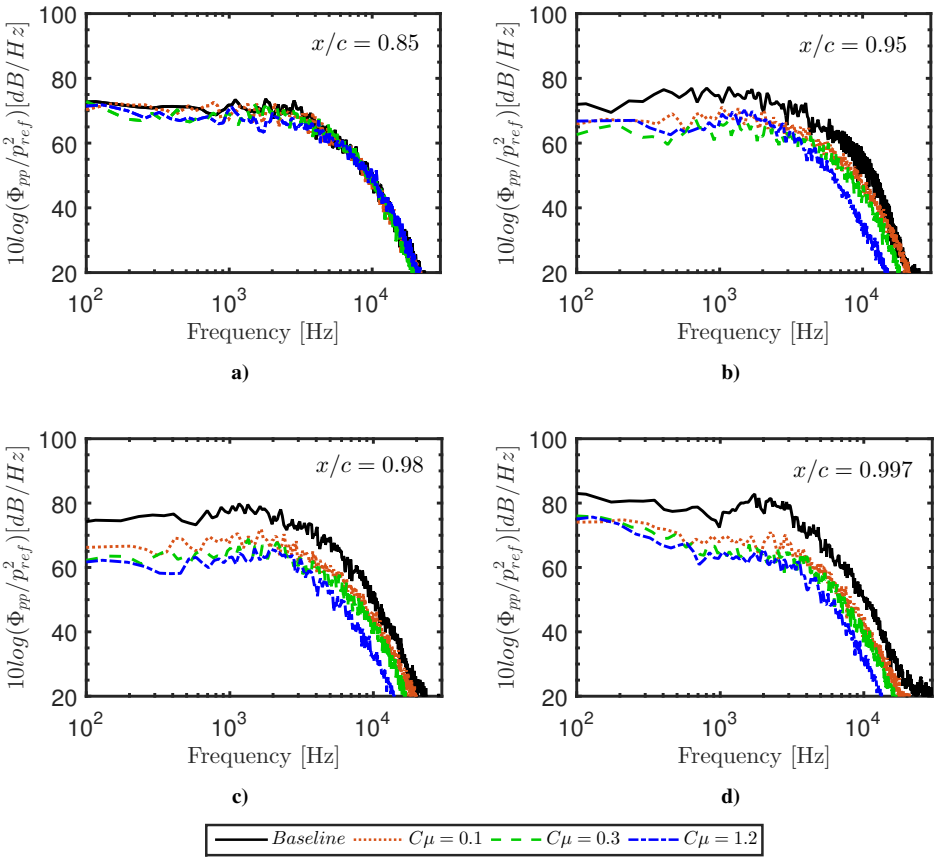

Figure 13. Power spectral density of the surface pressure probes at various streamwise locations for the NACA 0012 airfoil for baseline — and FS - - -.

4. Wall Pressure Spectra

The wall-pressure power spectral density (PSD) for points at the trailing edge on the suction side of the airfoil are presented in Fig. 13. The PSD was obtained by Fourier transformation using Hanning window, an overlap of 30% and performing the average eight times. The reference pressure used for the calculations is $P_{ref} = 2 \times 10^5$. The spectrum for the baseline shows a typical broadband behavior that arises from the interaction of turbulent boundary layers with the airfoil trailing edge. The PSD for the FS cases in comparison with the Baseline for various streamwise locations are shown in Fig. 13. At the location $x/c = 0.85$ (upstream of the FS slot), the Case 2 and 3 pressure spectra with suctions rates of $C_\mu = 0.3$ and 1.2 present lower values than that of the Baseline, this effect is more noticeable between low to mid-range frequencies ($300 < f < 2000$ Hz). At location $x/c = 0.95$, an overall reduction among all the three FS cases of about 10 dB in comparison with the Baseline were observed at a low to mid-range frequencies. At high frequencies, the reductions in the pressure spectra were more prominent as the intensity of the suction rates increased. A diminution of about 7 dB for $C_\mu = 0.1$, 10 dB for $C_\mu = 0.3$ and 17 dB for $C_\mu = 1.2$ were observed. At location $x/c = 0.98$, the most austere suction rate ($C_\mu = 1.2$) shows a reduction of about 16 dB while the case with the lowest suction rate ($C_\mu = 0.1$) resulted in a reduction of around 10 dB for low to mid-range frequencies. In the vicinity of the trailing edge at location $x/c = 0.997$, an overall reduction of around 10 dB for low to mid-frequencies was observed with no considerable differences among the different FS suction rates. However, for mid to high frequencies this difference becomes more prominent. The reduction reached by the highest FS suction rate (Case 3) is twice of the lowest FS suction rate (Case 1).

The temporal velocity signals acquired at various streamwise locations $x/c = 0.85, 0.95, 0.98$ and 0.997 for the Baseline and the FS cases are presented in Fig 14. At location $x/c = 0.85$ in Fig. 14a (upstream of the FS slot) the boundary layer turbulence from the tripping device is evident for the Baseline and the FS cases. The influence of the flow suction slot can be seen for the FS cases where an increase in the mean value of the non-dimensionalised velocity fluctuation can be observed as the intensity of flow suction increases. At the location x/c = 0.95 in Fig. 14b (just

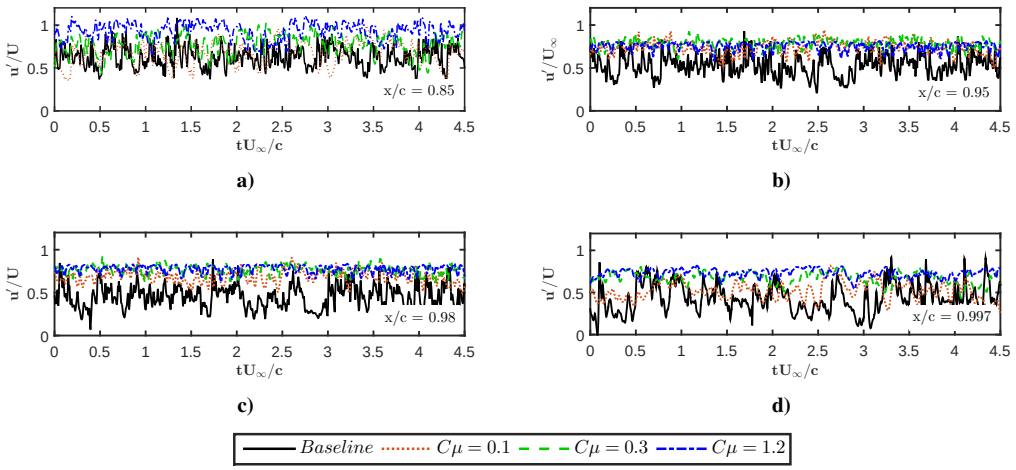

Figure 14. Time series of streamwise velocity fluctuations at various streamwise locations for the Baseline and FS cases.

downstream of the flow suction slot) a significant reduction in the velocity fluctuations were observed for the FS cases relative to the Baseline. The turbulence level reduces for all the FS cases. The mean values of the non-dimensionalised velocity fluctuations of the FS cases in comparison with the Baseline increases while the RMS values decreased as the intensity of the flow suction is increased. As the flow moves further downstream close to the trailing edge at the location $x/c = 0.997$, lower frequency and higher amplitudes of the non-dimensionalised velocity fluctuation were noticed for all the FS cases. The flow continues to develop and reach the trailing edge with reduced energy for all the FS cases relative to the Baseline.

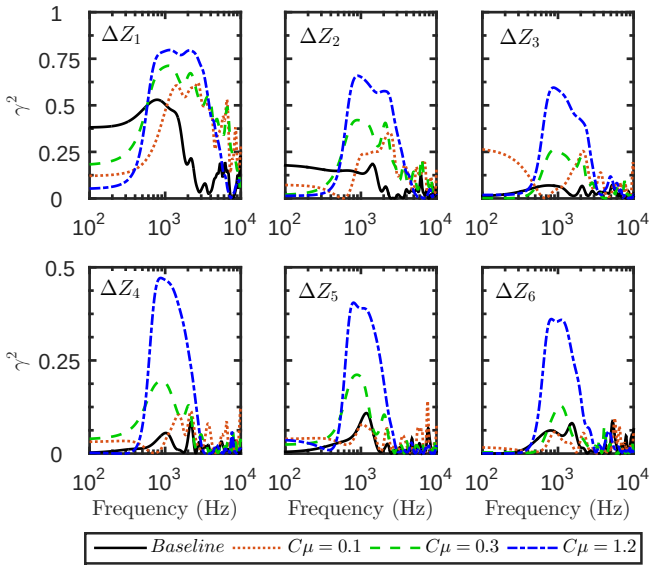

Figure 15. Spanwise coherence length for the Baseline and FS cases at streamwise location $x/c = 0.997$

The prediction of the sound pressure radiated by the full span width is assessed by the spanwise coherence, which is presented in Fig. 15 for six different measurement probe combinations along the span at streamwise location $x/c = 0.997$. The coherence was calculated between six following probes p_{1-2}, $p_{1-3...6}$ where, p_1 is the probe at the mid span of the domain. The respective distances between the probes are $\Delta Z_{1,2,3...6} = 0.624$ mm, 1.25 mm, 1.87 mm , 2.50 mm, 3.12 mm and 3.75 mm.

The spanwise coherence is defined in the Equation 2 as:

$$\gamma^2(Z, \Delta Z, f) = \frac{|\phi_{pp}(Z, \Delta Z, f)|^2}{|\phi_{pp}(Z, 0, f)||\phi_{pp}(Z + \Delta Z, 0, f)|} \tag{2}$$

where ϕ_{pp} is the cross-spectrum function which is calculated by the Fourier transform of the space-time cross-correlation function shown in Equation 3:

$$\phi_{pp}(Z, \Delta Z, f) = \int_{-\infty}^{\infty} \langle p(Z, t)p(Z + \Delta Z, t + \tau)\rangle e^{-if\tau}\, \mathrm{d}\tau \tag{3}$$

The spanwise coherence is related to the size of the turbulent flow structure. At low-frequency range the ΔZ_1 and ΔZ_2 plots (see Fig. 15) show the reduction in the coherence levels for all the FS cases compared to the Baseline. Since the large eddies in the flow are associated to low frequencies, the reduction on the coherence values for the FS cases can be associated with the reduction of the boundary layer thickness, mentioned earlier in Fig. 9a and the consequent decrease of the size of the flow structures within the boundary layer. At the mid-frequency range it was observed that for the six probe separation distances (see Fig. 15) the coherence values increased for all the FS cases in comparison with the Baseline. Since the scales of the dominant flow structures are of the same order as that of the boundary layer thickness, the smaller the boundary layer thickness the higher the frequency, which are related to the higher coherence values. The spanwise correlation length which is presented in Fig. 16 is calculated from the coherence function in the following Equation 4.

$$l_y(\omega) = \int_0^{\infty} \sqrt{\gamma^2(Z, \omega)}\mathrm{d}Z \tag{4}$$

where ω is frequency and z is the spanwise space among the measurement probes. A total of 64 probes were placed along the span and for the calculation of the spanwise correlation length, 17 probes equally-spaced along half-span starting from the mid-span were used for the final calculations. Figure 16 shows the spanwise coherence length at streamwise location $x/c = 0.997$. The correlation length reduces for all the FS cases relative to the Baseline for low-frequency range ($f < 400$ Hz). At frequencies higher than $f > 1$ kHz the FS cases present higher coherence lengths than that of the Baseline. This effect might be due to the smaller boundary layer thickness and lower turbulence levels.

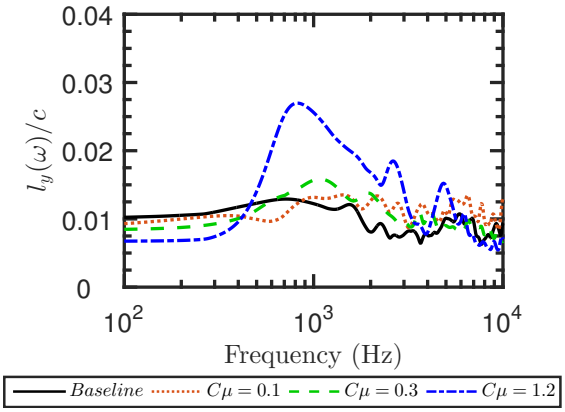

Figure 16. Length scale of the coherent flow structure for the Baseline and FS cases at streamwise location $x/c = 0.997$.

The aeroacoustic far-field predictions for the Baseline and the FS cases were calculated using Curle's aeroacoustic analogy [25] implemented in openFOAM [26]. The sound pressure level (SPL) for an observer located at $7.9c$ above the trailing edge is presented in Fig. 17. The results show reductions in the SPL for all the FS cases compared to the Baseline. The SPL decreases for the entire frequency range with higher mitigation at low to mid frequencies. At frequency $f = 300$ Hz, relative to the Baseline, a reduction in the SPL of up to 14 dB for the FS Case 1 and 24 dB for the Case 3 were observed. At mid-frequency range, $f = 2$ kHz reductions in the SPL of up to 8 dB and 17 dB for the FS Case 1 and Case 3 respectively relative to the Baseline was observed.

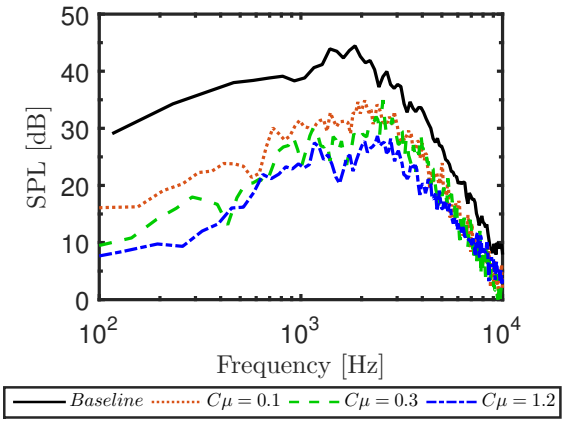

Figure 17. Far-field sound levels predicted using Curle's analogy, sound pressure level in dB reference to 2×10^5 Pa, at a distance with a radius of $r = 7.2c$ about the trailing-edge point at $90°$.

IV. Conclusion

A comprehensive study on the application of boundary layer suction for reducing trailing edge noise has been carried out. Large eddy simulations were performed for the symmetric NACA 0012 airfoil at the angle of attack $\alpha = 0°$ for a chord-based Reynolds number of $Re = 4 \times 10^5$ with and without trailing-edge flow suction (FS) having different flow suction rates. The results from the Baseline airfoil were thoroughly validated against the existing experimental data [21]. Results were presented for steady and unsteady pressure, boundary layer velocity profiles, wake velocity profiles, turbulent kinetic energy, Reynolds stresses, Q-criterion, coherence of the pressure, power spectral density and sound pressure levels. The results of the unsteady surface pressure for the FS cases show a significant broadband reduction at locations near the trailing edge relative to the Baseline case. The magnitude of the velocity deficit in the wake region has also been observed to reduce for the FS cases. The turbulent kinetic energy had increased by about 33 % for the FS case relative to the Baseline at streamwise location $x/c = 1.010$. The streamwise Reynolds stresses significantly reduced along the airfoil and in the wake region. The crosswise Reynolds stresses have shown to fade away along the airfoil while a peak appeared in the near wake. The Q-criterion has shown more coherent structures and lower vorticity. The coherent structures have shown to significantly increase at the location $x/c = 0.997$. The power spectral density of the wall-pressure results has shown an overall reduction in the broadband noise for various regions along the airfoil at various downstream locations aft of the flow suction region. The aeroacoustic far-field prediction using Curle's acoustic analogy has shown up to 24 dB reduction at low-mid range frequency for cases with the FS. The far-field noise results showed higher noise attenuation for $C_\mu = 1.2$, however, the $C_\mu = 0.1$ with only 8% of the flow suction rate of the $C_\mu = 1.2$ has achieved a noise reduction of about 58% of that achieved by $C_\mu = 1.2$. This showed that with a small amount of energy expenditure significant noise suppression can be achieved.

References

[1] Brooks, T. F., D. S. Pope, and M. A. Marcolini. "Airfoil self-noise and Prediction." NASA Reference Publication, No. 1218 (1989).

[2] Liu, X., Kamliya Jawahar, H., Azarpeyvand, M., and Theunissen, R. "Aerodynamic Performance and Wake Development of Airfoils with Serrated trailing edges", AIAA Journal, Vol. 55, No. 11 (2017), pp: 3669-3680.

[3] Liu, X., Kamliya Jawahar, H., Azarpeyvand, M., and Theunissen, R., "Aerodynamic and Aeroacoustic Performance of Serrated airfoils", AIAA 2015-2201, 2015.

[4] Liu, X., Kamliya Jawahar, H., Azarpeyvand, M., and Theunissen, R., "Wake Development of airfoils with Serrated Trailing Edges", AIAA 2016-2817, 2016.

[5] Lyu, B., Azarpeyvand, M., and Sinayoko, S., "Prediction of Noise from Serrated Trailing Edges", *Journal of Fluid Mechanics*, Vol. 793, pp: 556-588, 2016.

[6] Ai, Q., Azarpeyvand, M., Lachenal, X., and Weaver, P., "Aerodynamic and Aeroacoustic Performance of Airfoils Using Morphing Structures", *Wind Energy*, Vol. 19, No. 7, pp:1325-1339, July 2016.

[7] Kamliya Jawahar, H., Ai, Q., and Azarpeyvand, M., "Experimental and Numerical Investigation of Aerodynamic Performance of Airfoils with Morphed trailing edges", Renewable Energy, Vol. 127, (2018), pp: 355-367.

[8] Ai, Q., Kamliya Jawahar, H., and Azarpeyvand, M., "Experimental Investigation of Aerodynamic Performance of Airfoils Fitted with Morphing trailing edges", AIAA 2016-1563, 2016.

[9] Kamliya Jawahar, H., Azarpeyvand, M., and Carlos R.Ilario. "Experimental Investigation of Flow Around Three-Element High-Lift Airfoil with Morphing Fillers", AIAA 2017-3364, 2017.

[10] Kamliya Jawahar, H., Ai, Q., and Azarpeyvand, M., "Experimental and Numerical Investigation of Aerodynamic Performance of Airfoils Fitted with Morphing trailing edges", AIAA 2017-3371, 2017.

[11] Showkat Ali, S. A., Liu, X., and Azarpeyvand, M., "Bluff Body Flow and Noise Control Using Porous Media", AIAA 2016-2754, 2016.

[12] Showkat Ali, S. A., Szoke, M., Azarpeyvand, M., and Ilario, C., "Trailing edge Bluntness Flow and Noise Control Using Porous Treatments", AIAA 2016-2832, 2016.

[13] Showkat Ali, S. A., Szoke, M., Azarpeyvand, M., and Ilario, C., "Experimental Study of Porous Treatment for Aerodynamic and Aeroacoustic Purposes", AIAA 2017-3358, 2017.

[14] Szoke, M., and Azarpeyvand, M. "Active Flow Control Methods for the Reduction of Trailing Edge Noise", AIAA 2017-3004, 2017.

[15] Kral, L.D. "Active Flow Control Technology", ASME Fluids Engineering Division Technical Brief", ASME, 2000.

[16] Zha, G. C., Carroll, B. F., Paxton, C. D., Conley, C. A., and Wells, "High Performance Airfoil Using Co-Flow Jet Flow Control", AIAA Journal, Vol. 45, No. 8(2007), pp. 2087-2090 .

[17] Sellars, N. D., Wood, N. J., and Kennaugh, A., "Delta Wing Circulation Control Using the Coanda Effect, AIAA 2002-3269, 2002.

[18] Cagle, C. M., and Jones, G. S., "A Wind Tunnel Model to Explore Unsteady Circulation Control for General Aviation Applications", AIAA 2002-3240, 2002.

[19] Jones, G. S., and Englar, R. J., "Advances in Pneumatic-Controlled High-Lift Systems Through Pulsed Blowing", AIAA 2003-3411, 2003.

[20] Winkler J., Moreau S., and Carolus T., "Airfoil trailing edge Blowing: Broadband Noise Prediction from Large-Eddy Simulation", *AIAA Journal*, Vol. 50, No. 2, pp: 294-303, 2012.

[21] Garcia-Sagrado, Ana, and Tom Hynes. "Stochastic Estimation of Flow near the Trailing-edge of a NACA0012 Airfoil." Experiments in fluids 51.4 (2011): 1057.

[22] Wolf, William R., Joo Luiz F. Azevedo, and Sanjiva K. Lele. "Convective Effects and the Role of Quadrupole Sources for Aerofoil Aeroacoustics." Journal of Fluid Mechanics 708 (2012): 502-538.

[23] Yu, C., Wolf, W. R., Lele, S. K. "Airframe Noise Predictions using Large Eddy Simulation. Tech. Rep. High Performance Computing Conference, 2010.

[24] Lilly, Douglas K. "A proposed modification of the Germano subgridscale closure method." Physics of Fluids A: Fluid Dynamics 4.3 (1992): 633-635.

[25] Curle, N. "The influence of solid boundaries upon aerodynamic sound." Proceedings of the Royal Society of London A: Mathematical, Physical and Engineering Sciences. Vol. 231. No. 1187. The Royal Society, 1955.

[26] Kamliya Jawahar H., Lin Y., and Savill M., "Large Eddy Simulation of Airfoil Self-noise using OpenFOAM", *Aircraft Engineering and Aerospace Technology*, Vol. 90, No.1, pp: 126-133, 2018.